Evolution of laser induced electromagnetic postsolitons in multi-species plasma

Yue Liu, Ondřej Klimo, Timur Zh. Esirkepov, Sergei V. Bulanov, Yanjun Gu, Stefan Weber, and Georg Korn

Citation: Physics of Plasmas **22**, 112302 (2015); doi: 10.1063/1.4935303
View online: http://dx.doi.org/10.1063/1.4935303
View Table of Contents: http://scitation.aip.org/content/aip/journal/pop/22/11?ver=pdfcov
Published by the AIP Publishing

Evolution of laser induced electromagnetic postsolitons in multi-species plasma

Yue Liu,[1,a)] Ondřej Klimo,[1,2] Timur Zh. Esirkepov,[3] Sergei V. Bulanov,[3] Yanjun Gu,[1] Stefan Weber,[1] and Georg Korn[1]
[1]*Institute of Physics of the ASCR, ELI-Beamlines Project, Na Slovance 2, Prague 18221, Czech Republic*
[2]*FNSPE, Czech Technical University in Prague, Prague 11519, Czech Republic*
[3]*Advanced Photon Research Center, Japan Atomic Energy Agency, 8-1-7 Umemidai, Kizugawa, Kyoto 619-0215, Japan*

(Received 10 August 2015; accepted 11 October 2015; published online 9 November 2015)

The evolution of an s-polarized relativistic electromagnetic soliton created in multi-species plasma by an intense short laser pulse is investigated using two-dimensional particle-in-cell simulations. The multi-component plasma consists of electrons and high-Z ions with a small addition of protons. By comparison, the evolution of postsoliton is very different from that in hydrogen plasma. A halo-like structure is found in spatial patterns of both electromagnetic fields and electron densities. The process of energy depletion is much slower due to the smaller charge-to-mass ratio of ions, which implies a better way of detecting postsolitons in simulations and experiments. In addition, it is found that the Coulomb explosion of high-Z ions in the postsoliton stage facilitates low-Z ion acceleration, and the maximum energy of low-Z ions increases with the component ratio of high-Z to low-Z ions. © *2015 AIP Publishing LLC*. [http://dx.doi.org/10.1063/1.4935303]

I. INTRODUCTION

A relativistic electromagnetic (EM) soliton is a localized structure in collisionless plasma. In the electron density distribution, it has a cavity surrounded by a shell with a higher density. A low-frequency electromagnetic wave is trapped in the cavity, which is similar to a cavity resonator. The essentially relativistic electron motion is strongly coupled with the trapped electromagnetic mode, so that both particles and fields contribute equally to the total energy of the soliton. The analytical theory of relativistic electromagnetic solitons with a large amplitude is developed mainly in the framework of one-dimensional (1D) relativistic electron fluid approximation.[1–9] For the small amplitude solitary waves, the Korteweg-de Vries (KdV) equation can be applied.[10,11] Furthermore, initial-value problem of the KdV equation for the prediction of exact solitons has been attempted.[12,13]

The formation of relativistic electromagnetic solitons has been predicted using particle-in-cell (PIC) simulations of a relativistically strong short laser pulse interaction with underdense[14] and overdense[15] plasmas. In 1D configuration, circularly or linearly polarized solitary waves have been observed in correlation with the laser polarization.[16,17] Based on PIC simulations, it has also been proposed that these solitons can be generated by the nonlinear Bernstein-Greene-Kruskal (BGK) mode attained from an electron beam instability.[18] In general, the mechanism of soliton formation is related to the decrease of the local carrier frequency of the laser pulse spending energy on wake waves during its propagation in plasma.[19] This process produces sub-cycle solitons, only with enough room for a half of the spatial period of electromagnetic field.[1,3] The resulting soliton frequency, ω_S, is below the local Langmuir frequency, $\omega_{pe} = (4\pi e^2 n_e/m_e)^{1/2}$, where n_e is the electron density and e and m_e are the electron charge and mass, respectively. The soliton frequency and size, D_S, depend on the dimensionless amplitude of the soliton, $a_S = eE_S/m_e\omega_S c$, where E_S is the electromagnetic field strength and c is the speed of light in vacuum. In the limit of a small amplitude, $a_S \ll 1$, $\omega_{pe} - \omega_S \sim a_S^2$, and $D_S \sim a_S^{-1}$, while for large amplitudes, $a_S \gg 1$, the soliton frequency and size decrease following $\omega_S \sim a_S^{-1/2}$ and $D_S \sim a_S^{-1/2}$, respectively.[20]

Multi-dimensional PIC simulations revealed the structure and properties of relativistic electromagnetic solitary waves.[21–24] In a two- (2D) and three-dimensional (3D) configuration or in 1D linearly polarized case, even in a pure electron fluid approximation, the related solitary structures are not solitons *sensu stricto*, because they emit electromagnetic radiation (with frequencies higher than ω_S) and thus lose energy. Nevertheless, the term "soliton" is widely used for brevity. In these structures, the electron shell surrounding the cavity oscillates with the double frequency, $2\omega_S$, corresponding to two extrema of the electric field in the period $2\pi/\omega_S$.

Relativistic electromagnetic solitons stay or drift with a constant velocity in uniform plasma,[2,19] while in inhomogeneous plasma they move with acceleration against the density gradient[21] and eventually they transform into electromagnetic wavepackets. On an ion time-scale, solitons decay via the so-called postsoliton stage, finally transferring the energy to ions. It has been shown that the soliton formation is a significant channel of short laser pulse energy transformation.[19,25] Therefore, the relativistic electromagnetic solitons play an important role in relativistic laser plasma interactions.[26]

In experiments of terawatt (TW) femtosecond (fs) laser pulse interaction with plasmas, signatures of relativistic

[a)]Electronic mail: yue.liu@eli-beams.eu

electromagnetic solitons have been observed. The characteristic low-frequency radiation from solitons has been detected.[27] Postsolitons have been found by the proton radiography technique.[28–31]

The paper is organized as follows. The setup of the simulations is given in Sec. II. In Sec. III, we discuss the formation process of an s-polarized relativistic electromagnetic soliton created in hydrogen plasma. In Sec. IV, we investigate the evolution of postsoliton in a multi-component plasma consisting of electrons and high-Z ions with a small addition of protons by comparing it with that produced in pure hydrogen plasma. It is shown that the dissipation process of soliton energy is slower and more stable in multi-species case in Sec. V. In Sec. VI, the role of high-Z ions in the proton energy is emphasized. Studies show that Coulomb explosion of high-Z ions in the postsoliton stage will facilitate the acceleration of low-Z ions. Finally, the conclusions are given in Sec. VII.

II. SIMULATION SETUP

We perform 2D3V PIC simulations of the laser-plasma interaction using the code EPOCH.[32] The time, length, velocity, and electron density are normalized by the laser period T_L, wavelength λ_L, speed of light in vacuum c, and the critical density $n_{cr} = m_e\omega_L^2/4\pi e^2$, respectively. Here, e and m_e are the electron charge and mass, respectively, and $\omega_L = 2\pi/T_L = 2\pi c/\lambda_L$ is the laser frequency. The electric field strength E is characterized in terms of the dimensionless amplitude, $a = eE/m_e c\omega_L$, corresponding to the intensity of $I = E^2 c/4\pi \approx 1.37 \times a^2 \times 10^{18}\,\mathrm{W/cm^2} \times (1\mu\mathrm{m}/\lambda_L)^2$ for linearly polarized laser pulses.

The simulation box has a size of $60\,\lambda_L$ along the x direction (which is the direction of the laser pulse propagation) and $30\,\lambda_L$ along the y direction. The spatial resolution is 16 nodes per wavelength in each direction. The time step is about $0.042\,T_L$. The laser pulse is s-polarized and has Gaussian profile in both x and y directions. The pulse length is $l_x = 4\,\lambda_L$, while its spot size is $l_y = 5\,\lambda_L$. The dimensionless amplitude of the laser pulse is $a = 1$, corresponding to the intensity of 1.37×10^{18} W/cm^2 for the wavelength of $\lambda_L = 1\mu$m. Plasma occupies the interval of $5\,\lambda_L \le x \le 50\,\lambda_L$ along the x-axis; it spans the full y dimension of the simulation box. Plasma is homogeneous except the interval from $x = 5\,\lambda_L$ to $x = 10\,\lambda_L$, where it grows exponentially. In the homogeneous region, the electron density is $n_0 = 0.36\,n_{cr}$ corresponding to $4 \times 10^{20}\mathrm{cm}^{-3}$ for the wavelength of $\lambda_L = 1\mu$m. The corresponding Langmuir frequency is $\omega_{pe} = 0.6\,\omega_L$. In Section III, we consider hydrogen plasma, and further from Section IV, we also deal with plasma consisting of electrons, gold ions, and a relatively small fraction of protons. The total number of quasi-particles is approximately 1.38×10^6 for each species.

III. FORMATION OF AN S-POLARIZED SOLITON

Here, we start from an s-polarized soliton created by an intense laser pulse in underdense hydrogen plasma, consisting of electrons and protons.

In the left column of Fig. 1, we show the spatial distributions of electron densities with respect to their energy at different moments of time. In the middle and right columns, we

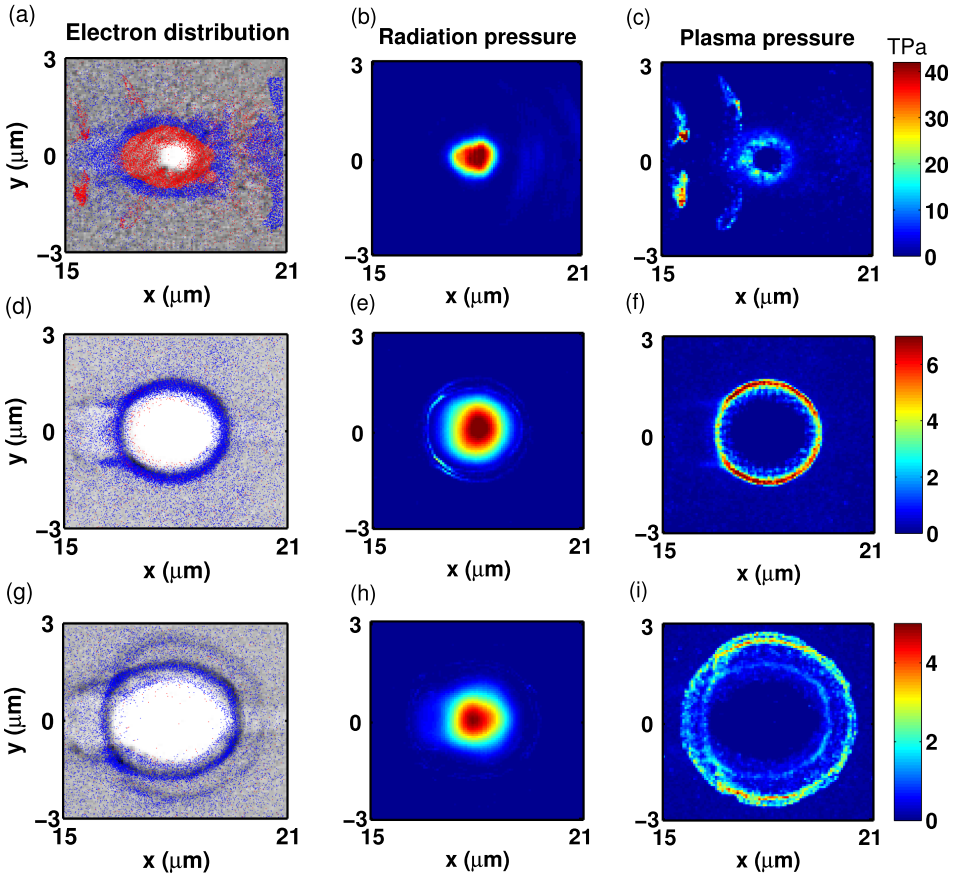

FIG. 1. The electron density (left column), radiation pressure (middle column), and plasma pressure (right column) at $t = 40\,T_L$ (upper row), $t = 80\,T_L$ (middle row), and $t = 120\,T_L$ (bottom row). In the left column, color corresponds to the electron energy, $\mathcal{E}$: red dots for $\mathcal{E} > 50$ keV and blue dots for 10 keV $< \mathcal{E} < 50$ keV.

plot the corresponding radiation pressure, $|E|^2/4\pi$, and plasma pressure, n_eT, respectively. Here, T is the isotropic temperature of electrons, which corresponds to the mean kinetic energy of electrons on grid in our simulations. At $t = 40\,T_L$, a large number of energetic electrons are observed inside the soliton, as seen in Fig. 1(a). Later, as seen in Figs. 1(d) and 1(g), electrons move outwards under the action of radiation pressure, which corresponds to the electromagnetic field trapped inside the cavity. As seen at $t = 80\,T_L$ and $t = 120\,T_L$, the number of electrons with the energy in the interval $10\text{keV} < \mathcal{E} < 50\text{keV}$ increases significantly. They oscillate near the postsoliton boundary, since they are pushed by the radiation pressure and attracted by the slowly expanding proton component of plasma at the same time. This produces an oscillating plasma pressure, shown in Figs. 1(c), 1(f), and 1(i). In Fig. 1(g), we also see an outer ring of electrons beyond the much denser boundary of postsoliton. The electron density of this ring is 40% greater than the background and the expansion velocity is $0.0125c$. These electrons move together with the most energetic protons, which are pushed away during the Coulomb explosion of the postsoliton. This process illustrates the formation principle of postsolitons from another point of view.

IV. COMPARISON OF POSTSOLITONS INDUCED IN HYDROGEN AND MULTI-SPECIES PLASMAS

In this section, we add the soliton formation and evolution in plasma consisting of electrons and gold ion with a small addition of protons. The target is a mixture of 90% Au^+, 10% protons (H^+), and electrons neutralizing the ions. Other parameters are the same as above.

Figures 2 and 3 show the spatial distributions of the transverse electric field component E_z at two different moments of time and the corresponding zoomed-in magnetic field component B_y at $t = 80\,T_L$ for two different kinds of plasmas. The first row in Fig. 2 shows the soliton in hydrogen plasma and the second row is for the case of the plasma with gold ion involved. We can see that the laser pulse propagates through plasma from the direction indicated by the black arrow and then creates a soliton at the position of $x = 18\,\lambda_L$. The transmitted laser pulse is modified so that a substantial phase shift appears in its central part, which corresponds to a ring laser pulse structure in 3D case.[23] During this process, we find over 30% of laser pulse energy is transferred to the soliton in hydrogen case. The electric field component oscillates with the frequency of $\omega_S = 0.4\,\omega_L$, lower than the Langmuir frequency of undisturbed plasma. In the soliton, magnetic field is azimuthal, i.e., the corresponding vector field encompasses the center of the soliton similarly to a vortex.[20] It is seen as a dipole structure in the distribution of the B_y component, which is shown in Fig. 3. The direction of rotation of this field oscillates with the soliton frequency. In Figs. 2 and 3, we observe a series of rings corresponding to the outgoing electromagnetic radiation. Due to this emission, solitons lose energy. It is obvious that the electromagnetic patterns of the soliton produced in two cases are different, especially for the moment $t = 80\,T_L$. We can find that at the edge of the postsoliton in multi-species plasma there is a halo-like structure and the frequency of the outgoing electromagnetic radiation is higher than that in hydrogen plasma. It is due to the fact that the electromagnetic field of the soliton in multi-species plasma is stronger and the frequency of the soliton is higher, too.

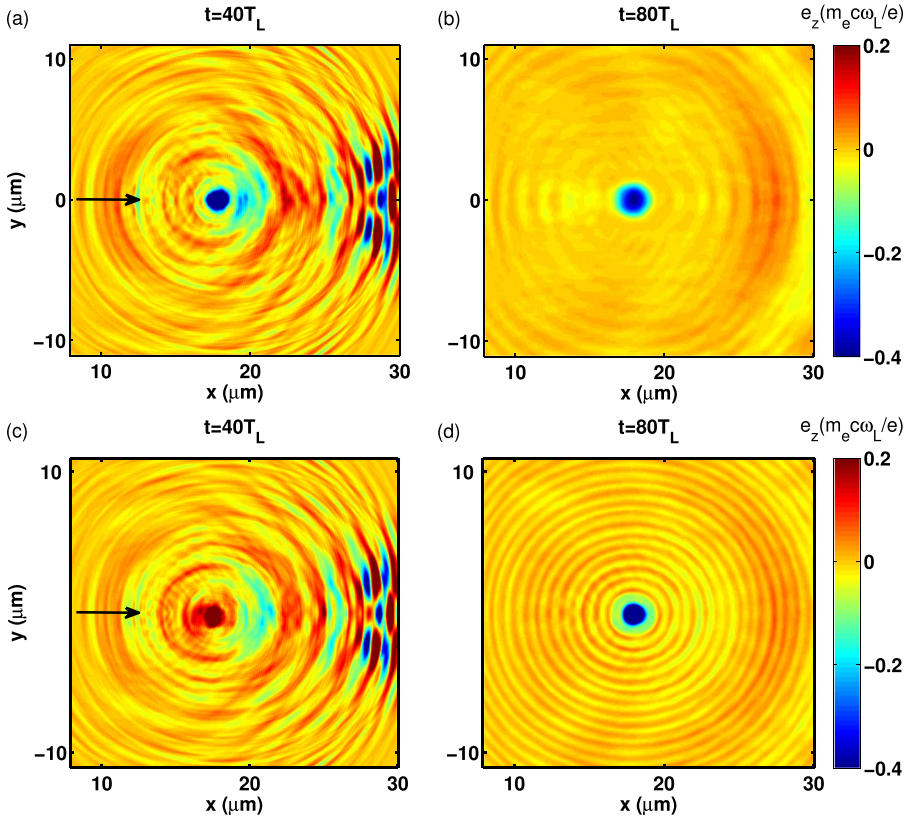

FIG. 2. The electric field E_z in hydrogen plasma (top row) and in multi-species plasma (bottom row) of the soliton in the (x, y) plane at $t = 40\,T_L$ ((a) and (c)) and at $t = 80\,T_L$ ((b) and (d)). The black arrow indicates the incident direction of the laser pulse.

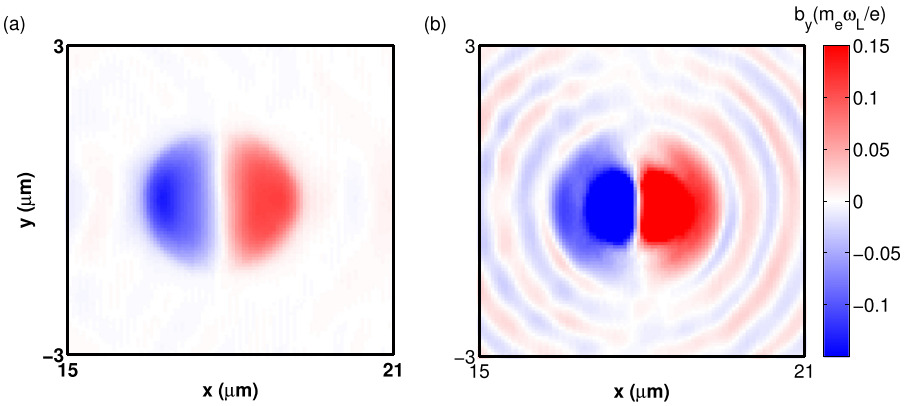

FIG. 3. The zoomed-in magnetic field B_y in hydrogen plasma (a) and in multi-species plasma (b) of the soliton in the (x, y) plane at $t = 80\,T_L$.

The electron densities of a soliton produced in hydrogen plasma and in multi-species plasma are shown in Fig. 4 at the moments of time $t = 40\,T_L$ and $t = 80\,T_L$. In Fig. 5, we plot the proton density in hydrogen plasma and the gold ion density in multi-species plasma at two moments of time. It needs to be pointed out that the spatial distribution of proton densities in multi-species plasma is the same as that in hydrogen plasma. By comparing them, we can see how the high-Z ion background with a low ionization state influences the formation and evolution of the soliton. We know that the $\mathbf{v} \times \mathbf{B}$ force in the soliton pushes the electrons outwards. Here, $\mathbf{v}$ is the electron velocity. Since the electromagnetic field oscillates with the frequency of ω_S, this force oscillates with the double frequency, $2\omega_S$. Therefore, the soliton boundary oscillates with the soliton frequency doubled, as has been observed earlier.[7,21] Eventually the uncompensated ion background in the soliton undergoes Coulomb explosion.[22] As a result, the soliton size increases and ions are accelerated. The plasma expansion is quasi-neutral, as seen in Fig. 4(b). The time-scale of this process is $\tau_i \approx 2\pi(m_i/m_e)^{1/2}\omega_{pe} = 70\,T_L$, where $m_i/m_e = 1836$ is the proton-to-electron mass ratio. The electromagnetic field continues to oscillate in the expanding soliton cavity with gradually decreasing frequency. This stage of the late evolution of a soliton has been called "postsoliton."[22]

Different from Fig. 4(b), the soliton size is almost the same as at the beginning in multi-species plasma at $t = 80\,T_L$. A halo in the electron density seen around the soliton corresponds to the structures of electromagnetic fields in Figs. 2(d) and 3(b). It can be easily found that the outer dense ring of the halo structure in the electron density distribution is consistent with the distribution pattern of its corresponding proton density. The Coulomb explosion of gold ions is much slower than that of protons, since the former is much heavier than the latter. Consequently, the corresponding hole in the gold ion density in Fig. 5(d) is barely seen. In contrast, protons are efficiently accelerated by the electrostatic potential of the soliton and maintained by the gold ions.

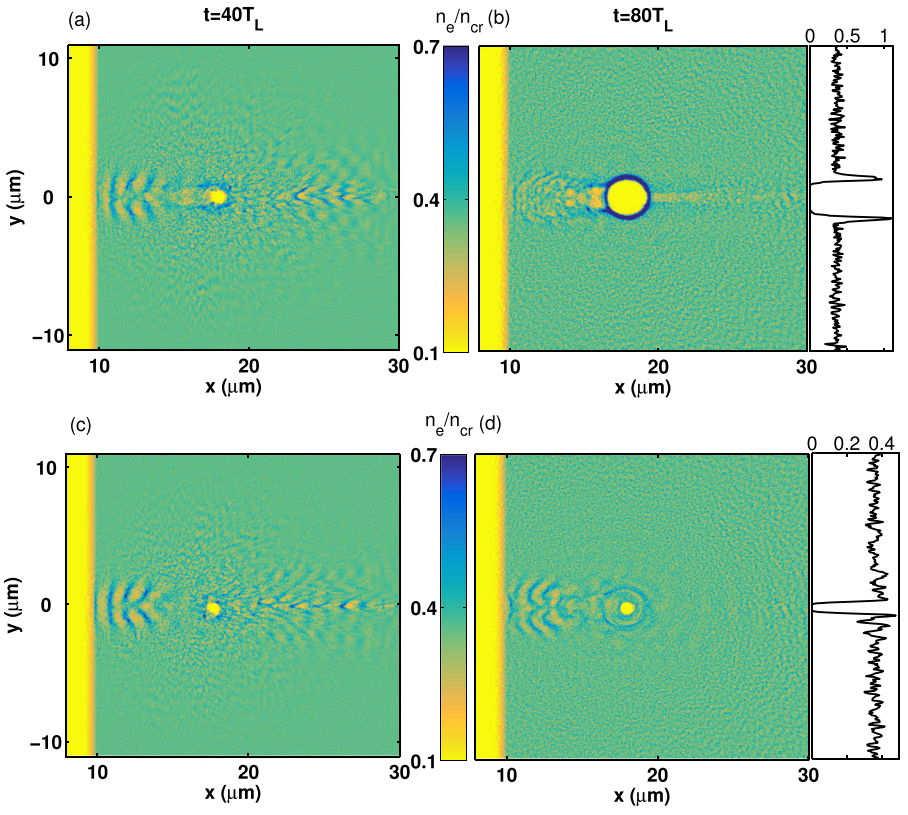

FIG. 4. The electron density n_e in hydrogen plasma (top row) and in multi-species plasma (bottom row) of the soliton in the (x, y) plane at $t = 40\,T_L$ ((a) and (c)) and at $t = 80\,T_L$ ((b) and (d)). The lineouts of the electron density at $x = 18\,\mu$m are shown for $t = 80\,T_L$.

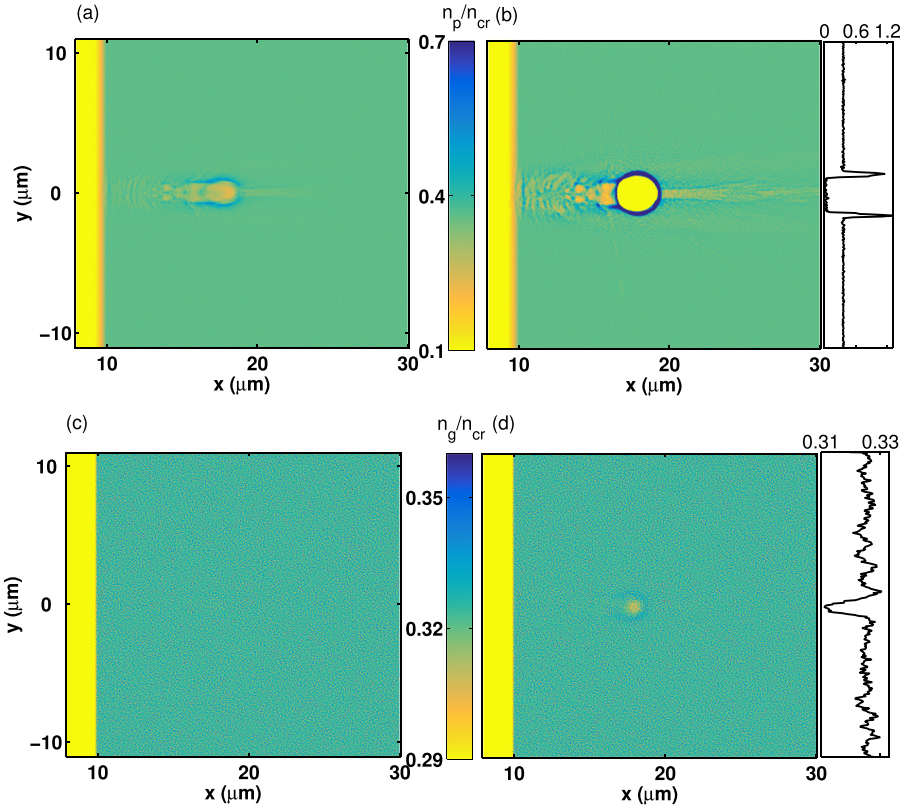

FIG. 5. The proton density n_p (top row) in hydrogen plasma and the gold ion density n_g (bottom row) in multi-species plasma in the (x, y) plane at $t = 40\,T_L$ ((a) and (c)) and at $t = 80\,T_L$ ((b) and (d)). The lineouts of the ion density at $x = 18\,\mu$m are shown for $t = 80\,T_L$.

Figure 6 shows the proton phase space projections onto the planes (y, p_y) and (x, p_y) at $t = 300\,T_L$ in two different plasmas. These patterns are typical to a Coulomb explosion of a compact object. The fastest ions are located in the outermost ring with a characteristic folding in the phase space which produces sharp edges in the corresponding density distributions, as seen in Fig. 5(b). It is shown that the proton phase space projections onto the planes (y, p_y) and (x, p_y) in multi-species plasma appear in the same pattern as in hydrogen plasma. However, substantially larger momenta are acquired by protons in multi-species plasma than in hydrogen plasma due to a longer life-time of the electric potential created by the gold ions.

V. TEMPORAL EVOLUTION OF POSTSOLITONS

We present the temporal waveform of the electric field E_z component at the center of the soliton in Fig. 7 for two cases. As can be easily seen, the amplitude of electric field of the soliton decreases in both cases. However, the

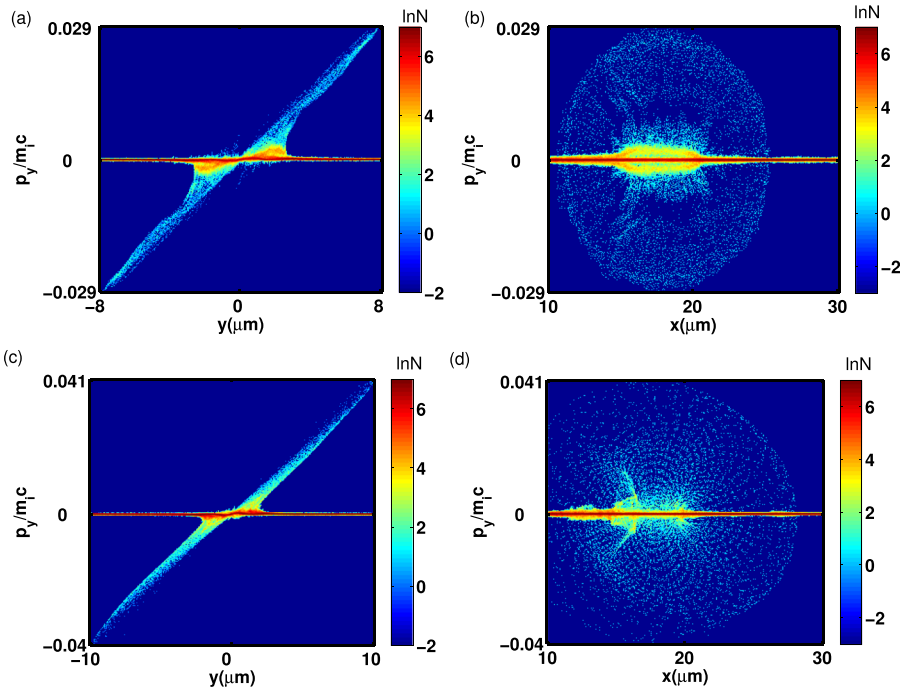

FIG. 6. Proton phase space distributions of the soliton. The ion momentum component p_y in units of m_ic versus the coordinates y and x in hydrogen plasma (top row) and in multi-species plasma (bottom row) at time $t = 300\,T_L$, where N stands for the number of quasi-particles.

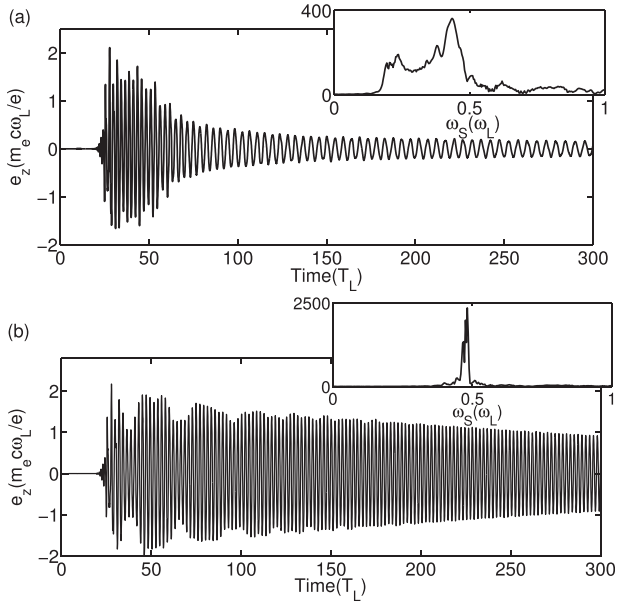

FIG. 7. Temporal evolutions of the transverse electric field E_z at the center of the soliton in hydrogen plasma (a) and in multi-species plasma (b) with its frequency spectrum over the whole time period in the inset, respectively.

amplitude goes down much more slowly in multi-species plasma. Besides, we can observe that the distance between consecutive nodes increases with time in Fig. 7(a), which means that the soliton frequency is gradually downshifted. Correspondingly, we can see a broad frequency spectrum over the whole time period in hydrogen case, while the frequency spectrum in multi-species case is quite localized. Therefore, it would be much easier to diagnose the postsoliton produced in multi-species plasma in experiments or simulations due to the stability in both its amplitude and its frequency. This provides us with a potential diagnostic method of postsolitons. In Fig. 8, we plot frequency spectra of the waveform shown in Fig. 7 taken in different time

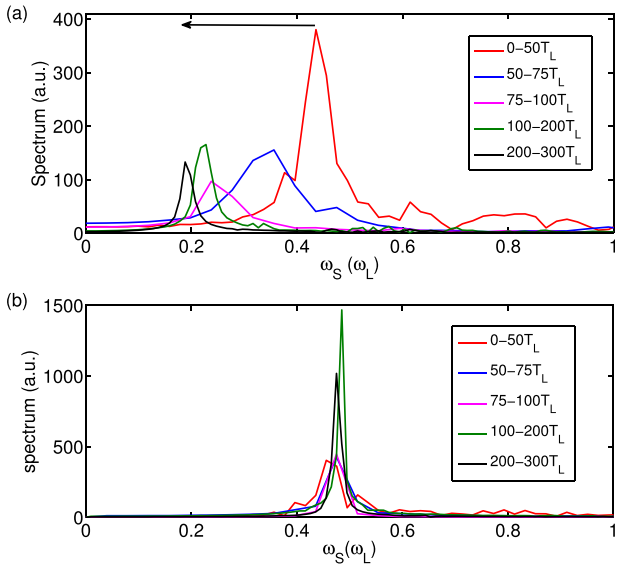

FIG. 8. Frequency spectra corresponding to five different time intervals in hydrogen plasma (a) and in multi-species plasma (b).

intervals. The main frequency drops from about $0.4\,\omega_L$ to around $0.2\,\omega_L$ for hydrogen case. We see that the rate of the soliton frequency downshift becomes slower with time. Higher frequencies are seen at the beginning. They are related to the soliton boundary oscillation and ringlike pattern of the outgoing electromagnetic radiation seen in Figs. 2 and 3. At the late stages of evolution, they fade out. On the other hand, in multi-species case, it is not easy to observe some particular trend of the piecewise frequency spectra. Under all circumstances, the frequency spectra are almost overlapped at around $0.47\,\omega_L$, which is even larger than the frequency in hydrogen case at the beginning. This explains in some way why the outgoing electromagnetic radiation in Fig. 2(d) has a much higher frequency than that in Fig. 2(b).

The snowplow model[22,33] has predicted that the frequency of the soliton evolves following the law $\omega_S \sim t^{-1/3}$ in hydrogen plasma. This is consistent with our results in Fig. 8(a), which shows the frequency of the soliton at time $t = 50\,T_L$ is around $0.35\,\omega_L$ and it falls to $0.19\,\omega_L$ at time about $t = 300\,T_L$.

In Fig. 9(a), we plot the time dependencies for different kinds of energy stored in the soliton induced in hydrogen plasma: the energy of electromagnetic fields, $\mathcal{E}_{EM} = \int d^3x\ (\mathbf{E}^2 + \mathbf{B}^2)/8\pi$, the kinetic energy of particles, $\mathcal{E}_{ep} = \sum(\gamma_e - 1)m_e c^2 + \sum(\gamma_p - 1)m_p c^2$, and the total soliton energy, $\mathcal{E}_{EM} + \mathcal{E}_{ep}$. Here, γ_e and γ_p are the Lorentz factors for electrons and protons, respectively. As soliton expands, and there is no much energy stored outside the soliton boundary; for simplicity, we compute the specified quantities in a disk with the radius of $5\,\lambda_L$, centered at the average location of the lowest electron density. At $t = 40\,T_L$, the soliton is formed and the laser pulse is already detached from the soliton, as seen in Fig. 2(a). At this moment, more than 30% of the initial laser energy is stored in the soliton. The inset in Fig. 9(a) show that at the beginning the oscillations of the energy of electromagnetic field and electrons are in antiphase. At this stage, both the electromagnetic field and electrons equally contribute to the total energy of the soliton, while the proton contribution is negligible. The antiphase oscillations reveal the process of periodical energy redistribution between fields and particles in the soliton. A fast dissipation of the soliton energy from $t = 30\,T_L$ to $40\,T_L$ occurs while the proton energy remains small. This indicates that the soliton loses energy mainly by means of the electromagnetic emission, as seen in Figs. 2 and 3. Starting from $t = 30\,T_L$, when the soliton is formed, protons slowly acquire energy. On the ion time-scale, approximately at $t = 60\,T_L$, the energy stored in protons becomes equal to that stored in electrons and fields. About this moment, the soliton transforms into postsoliton. Later, the proton energy growth becomes much slower. The energy of electromagnetic field becomes less than that of electrons, and both are less than the energy of protons. At $t = 70\,T_L$, only 8% of electromagnetic field energy remains in the postsoliton. At later stages, the electromagnetic field energy transforms mainly into energy of ions and is spent on the electromagnetic emission.

Likewise, Fig. 9(b) illustrates the temporal evolution of different components of the soliton energy in multi-species

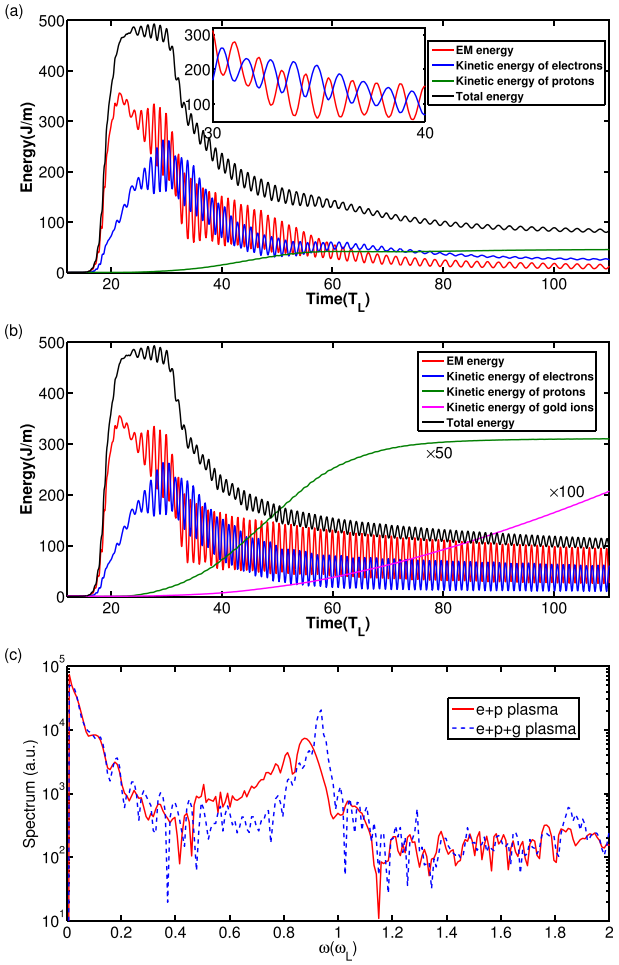

FIG. 9. Temporal evolutions of the electromagnetic energy (red), kinetic energy of particles (blue for electrons and dark green for protons), and the total energy (black) of a soliton in electron-proton plasma (a) and in multi-species plasma with kinetic energy of gold ions shown in purple color (b), with the kinetic energy of electrons and electromagnetic (EM) field over a time period from $t = 30\,T_L$ to $t = 40\,T_L$ in hydrogen case in the inset are shown. (c) Frequency spectra of the electromagnetic energy evolution (red lines in Figs. 9(a) and 9(b)) in hydrogen plasma (solid red line) and in multi-species plasma (dashed blue line).

plasma. Similar to the case of hydrogen plasma, the soliton formed in multi-species plasma obtains a large portion of the initial laser pulse energy. From about $t = 30\,T_L$ to $t = 40\,T_L$, both the electromagnetic field and electrons contribute to the total energy of the soliton equally, while the energy of all ions is negligible. The oscillations of the electromagnetic field energy and the electron kinetic energy are in antiphase as in the inset of Fig. 9(a). The soliton loses energy via emitting electromagnetic waves. At about $t = 50\,T_L$, the contribution from electrons on average becomes less than a half of the total soliton energy. Gold ions acquire energy very slowly due to their large inertia, while energy stored in protons is small because of their small number.

In Fig. 9(c), we show the frequency spectra corresponding to the dependence of electromagnetic field energies on time in Figs. 9(a) and 9(b). Considering that the energy of electromagnetic field is defined as a sum of squares of the electric and magnetic fields components, its oscillation frequency should be twice the frequency of field components. Therefore, we can divide the frequency of electromagnetic field energy by 2 in Fig. 9(c), in order to compare it with the frequency corresponding to electromagnetic field. In this way, we can obtain two frequency peaks at around $0.44\,\omega_L$ and $0.88\,\omega_L$ from the solid red line in hydrogen plasma, while two frequency peaks are found at $0.46\,\omega_L$ and $0.92\,\omega_L$ from the dashed blue line in multi-species plasma. The former corresponds to the soliton base frequencies, while the latter indicates the oscillations of the soliton boundary. These values are higher in multi-species case than in pure hydrogen case, because in multi-species plasma the soliton frequency downshifts much more slowly than in hydrogen plasma. We can find that the spectra of electromagnetic energy calculated over the whole soliton area in Fig. 9(c) are consistent with the frequency spectra of central electric field in Fig. 8 to some extent.

VI. ROLE OF HIGH-Z IONS IN THE PROTON ENERGY

Our simulations show that the involvement of heavy ions facilitates the acceleration of proton around the soliton. In Fig. 10, we compare the energy spectra of protons for the cases of hydrogen plasma and multi-species plasma. The protons gain substantially larger energy in the latter case. In electron-proton plasma, at time $t = 80\,T_L$, the maximum energy of protons is 0.41 MeV. At the same time in multi-species plasma, the maximum energy of protons reaches 0.82 MeV, which is exactly twice that of the protons in hydrogen plasma.

Figure 11 illustrates the maximum energy of protons as a function of different plasma compositions in electron-proton-gold plasma at time $t = 80T_L$. As we can see, there is a sharp increase of maximum proton energy with the component ratio of gold to hydrogen in the first place. When the ratio reaches one, the increase slows down and it shows a saturation trend afterwards. It means the protons of the soliton gain higher maximum energy when more heavy ions are mixed in multi-species plasma. Moreover, we plot the maximum proton energies with colorful squares when gold ions of higher ionization states are introduced. It turns out that the charge of heavy ions shows weak influence on the maximum energy of protons provided that the charge-to-mass ratio is extremely small.

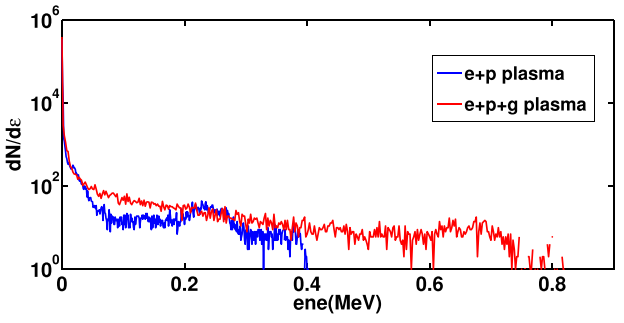

FIG. 10. The energy spectra of protons in electron-proton plasmas (blue line) and in electron-proton-gold plasma (red line) at time $t = 80\,T_L$.

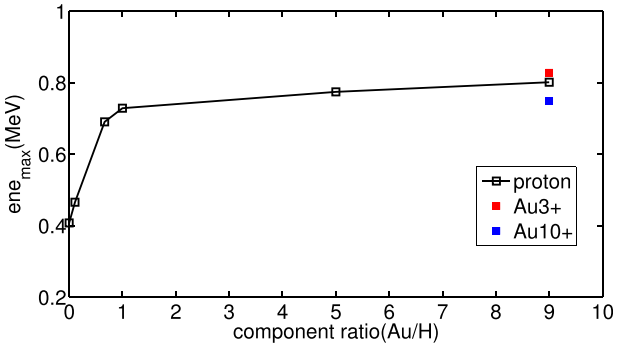

FIG. 11. The dependence of maximum energy of protons (square) on the component ratio (Au/H) in electron-proton-gold plasma (black line) at time $t = 80T_L$. Besides, we also check it by replacing the Au^+ with Au^{3+} (red solid square) and Au^{10+} (blue solid square).

VII. CONCLUSION

The evolution of relativistic electromagnetic solitons created by an intense short laser pulse in multi-species plasma consisting of high-Z ions with a low ionization state and a small fraction of protons is presented. Such a kind of postsoliton is compared with that produced in pure hydrogen plasma in terms of the distributions of electromagnetic field, particle density, particle phase space, and the evolutions of different energy components. It is known that a significant portion of laser pulse energy can be transformed into solitons, which eventually transfer their energy to ions. The fast energy depletion of s-polarized solitons is mainly due to their emission of electromagnetic waves. However, the depletion process of postsoliton is very slow in multi-species plasma, since the soliton life-time is determined by the high-Z ion-to-electron mass ratio. It provides us with a promising way of diagnosing postsoliton in simulations and experiments.

Long-lived electric potential created by high-Z ions in the soliton efficiently accelerates low-Z ions with the characteristic patterns of momentum distribution corresponding to Coulomb explosion. Furthermore, the acceleration process is optimized by increasing the high-Z ion components. Our results are also important for diagnostics of relativistically strong laser-plasma interactions exhibiting relatively energetic ions with isotropic spectra.

ACKNOWLEDGMENTS

This work has been financially supported by the ELI (Project No. CZ.1.05/1.1.00/02.0061). Computational resources were provided by the MetaCentrum under the Program No. LM2010005 and the CERIT-SC under the program Centre CERIT Scientific Cloud, part of the Operational Program Research and Development for Innovations, Reg. No. CZ.1.05/3.2.00/08.0144.

[1]J. H. Marburger and R. F. Tooper, Phys. Rev. Lett. **35**, 1001 (1975).
[2]V. A. Kozlov, A. G. Litvak, and E. V. Suvorov, Zh. Eksp. Teor. Fiz. **76**, 148 (1979) [Sov. Phys. JETP **49**, 75 (1979)].
[3]T. Zh. Esirkepov, F. F. Kamenets, S. V. Bulanov, and N. M. Naumova, JETP Lett. **68**, 36 (1998).
[4]D. Farina, M. Lontano, and S. V. Bulanov, Phys. Rev. E **62**, 4146 (2000).
[5]D. Farina and S. V. Bulanov, Phys. Rev. Lett. **86**, 5289 (2001).
[6]D. Farina and S. V. Bulanov, Plasma Phys. Controlled Fusion **47**, A73 (2005).
[7]G. Sánchez-Arriaga and E. Lefebvre, Phys. Rev. E **84**, 036403 (2011).
[8]G. Sánchez-Arriaga and E. Lefebvre, Phys. Rev. E **84**, 036404 (2011).
[9]G. Sánchez-Arriaga, E. Siminos, V. Saxena, and I. Kourakis, Phys. Rev. E **91**, 033102 (2015).
[10]H. Washimi and T. Taniuti, Phys. Rev. Lett. **17**, 996 (1966).
[11]A. P. Kakad, S. V. Singh, R. V. Reddy, G. S. Lakhina, and S. G. Tagare, Adv. Space Res. **43**, 1945 (2009).
[12]N. J. Zabusky and M. D. Kruskal, Phys. Rev. Lett. **15**, 240 (1965).
[13]C. S. Gardner, J. M. Greene, M. D. Kruskal, and R. M. Miura, Phys. Rev. Lett. **19**, 1095 (1967).
[14]S. V. Bulanov, I. N. Inovenkov, V. I. Kirsanov, N. M. Naumova, and A. S. Sakharov, Phys. Fluids B **4**, 1935 (1992).
[15]S. V. Bulanov, N. M. Naumova, and F. Pegoraro, Phys. Plasmas **1**, 745 (1994).
[16]A. Macchi, A. S. Nindrayog, and F. Pegoraro, Phys. Rev. E **85**, 046402 (2012).
[17]D. Wu, C. Y. Zheng, X. Q. Yan, M. Y. Yu, and X. T. He, Phys. Plasmas **20**, 033101 (2013).
[18]A. Kakad, Y. Omura, and B. Kakad, Phys. Plasmas **20**, 062103 (2013).
[19]S. V. Bulanov, T. Zh. Esirkepov, F. F. Kamenets, and N. M. Naumova, Plasma Phys. Rep. **21**, 550 (1995).
[20]S. V. Bulanov, T. Zh. Esirkepov, N. M. Naumova, F. Pegoraro, and V. A. Vshivkov, Phys. Rev. Lett. **82**, 3440 (1999).
[21]Y. Sentoku, T. Zh. Esirkepov, K. Mima, K. Nishihara, F. Califano, F. Pegoraro, H. Sakagami, Y. Kitagawa, N. M. Naumova, and S. V. Bulanov, Phys. Rev. Lett. **83**, 3434 (1999).
[22]N. M. Naumova, S. V. Bulanov, T. Zh. Esirkepov, D. Farina, K. Nishihara, F. Pegoraro, H. Ruhl, and A. S. Sakharov, Phys. Rev. Lett. **87**, 185004 (2001).
[23]T. Zh. Esirkepov, K. Nishihara, S. V. Bulanov, and F. Pegoraro, Phys. Rev. Lett. **89**, 275002 (2002).
[24]T. Esirkepov, S. V. Bulanov, K. Nishihara, and T. Tajima, Phys. Rev. Lett. **92**, 255001 (2004).
[25]M. Tushentsov, A. Kim, T. F. Cattani, D. Anderson, and M. Lisak, Phys. Rev. Lett. **87**, 275002 (2001).
[26]G. A. Mourou, T. Tajima, and S. V. Bulanov, Rev. Mod. Phys. **78**, 309 (2006).
[27]M. Kando *et al.*, AIP Conf. Proc. **1153**, 61 (2009).
[28]M. Borghesi, S. V. Bulanov, D. H. Campbell, R. J. Clarke, T. Zh. Esirkepov *et al.*, Phys. Rev. Lett. **88**, 135002 (2002).
[29]L. Romagnani, A. Bigongiai, S. Kar, S. V. Bulanov, C. A. Cecchetti *et al.*, Phys. Rev. Lett. **105**, 175002 (2010).
[30]G. Sarri, D. K. Singh, J. R. Davies, F. Fiuza, K. L. Lancaster *et al.*, Phys. Rev. Lett. **105**, 175007 (2010).
[31]F. Sylla, A. Flacco, S. Kahaly, M. Veltcheva, A. Lifschitz, G. Sánchez-Arriaga, E. Lefebvre, and V. Malka, Phys. Rev. Lett. **108**, 115003 (2012).
[32]C. P. Ridgers, J. G. Kirk, R. Duclous, T. G. Blackburn, C. S. Brady, K. Bennett, T. D. Arber, and A. R. Bell, J. Comput. Phys. **260**, 273 (2014).
[33]S. V. Bulanov and F. Pegoraro, Phys. Rev. E **65**, 066405 (2002).